Supporting Information

Neuron-like polyelectrolyte/carbon nanotube composites for ultra-high loading of metal nanoparticles

Md. Shahinul. Islam [a] , Won San Choi [b,*], Tae Sung Bae [c], Young Boo Lee [c] , Ha-Jin Lee [a,*]

[a] Western Seoul Center, Korea Basic Science Institute (KBSI), 150 Bugahyunro, Seodaemun-gu, Seoul 120-140, Republic of Korea

[b] Department of Chemical and Biological Engineering, Hanbat National University, 125 Dongseodaero, Yuseong-gu, Daejeon, 305-719, Republic of Korea

[c] Jeonju Center, Korea Basic Science Institute (KBSI), 20 Gunjiro, Dukjin-gu, Jeonju 561-180, Republic of Korea

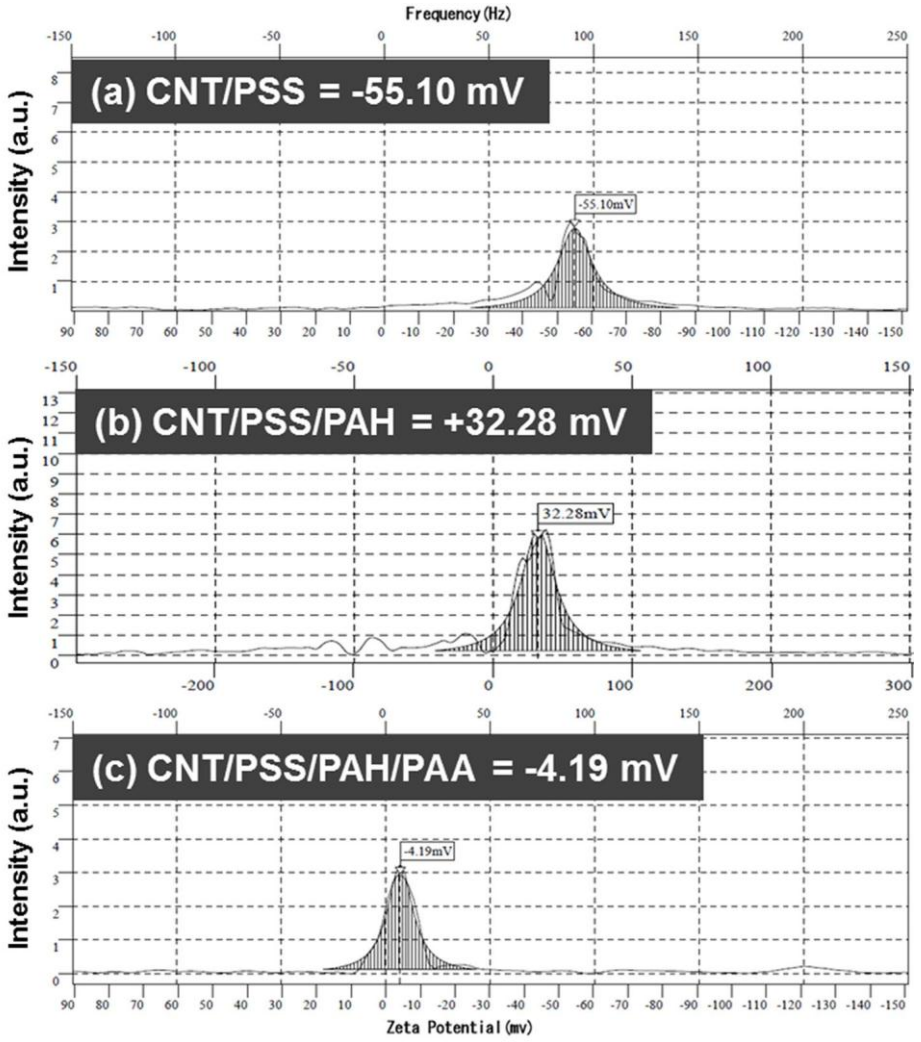

Figure S1. Zeta-potential data of PE-coated p-CNTs.

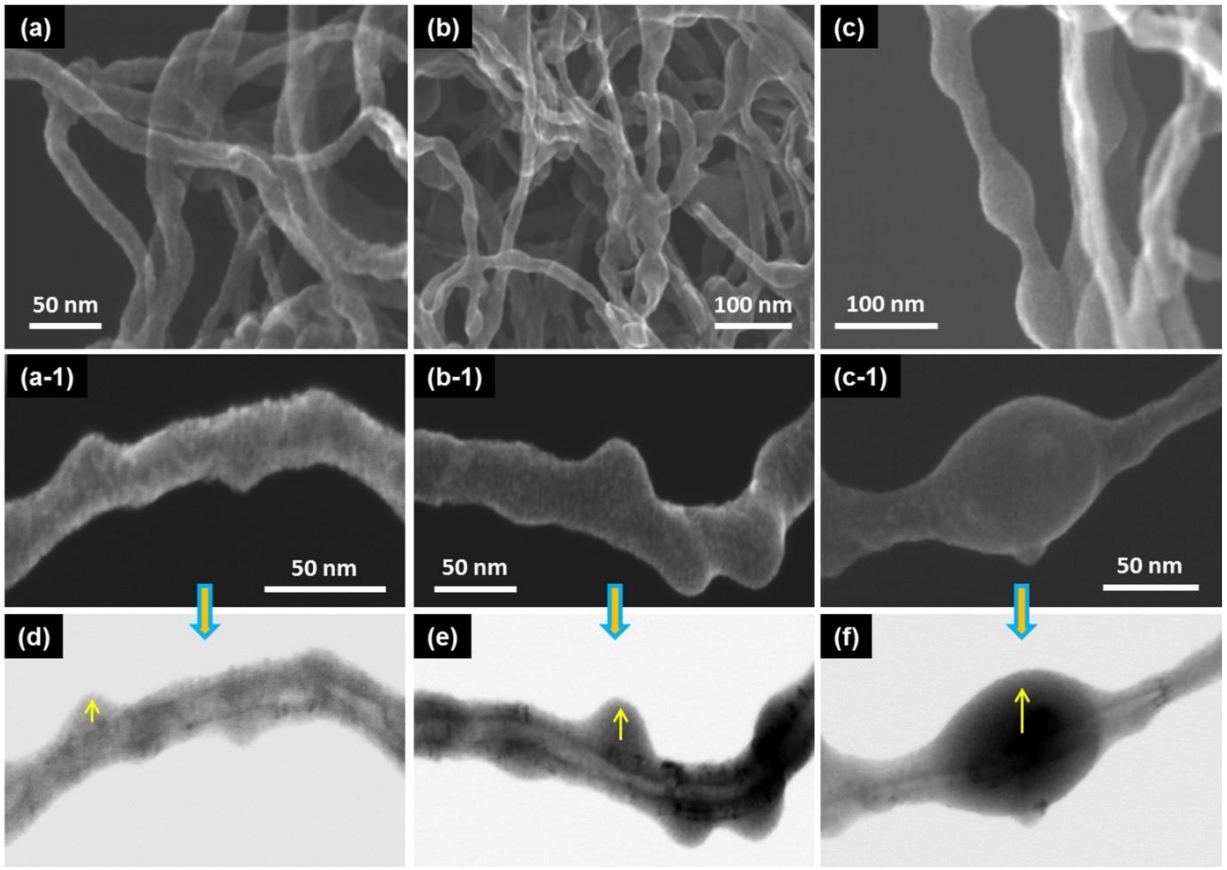

Figure S2. UHR-FESEM images of (a) p-CNT/PSS, (b) p-CNT/PSS/PAH and (c) p-CNT/PSS/PAH/PAA, and (d-f) the corresponding STEM images.

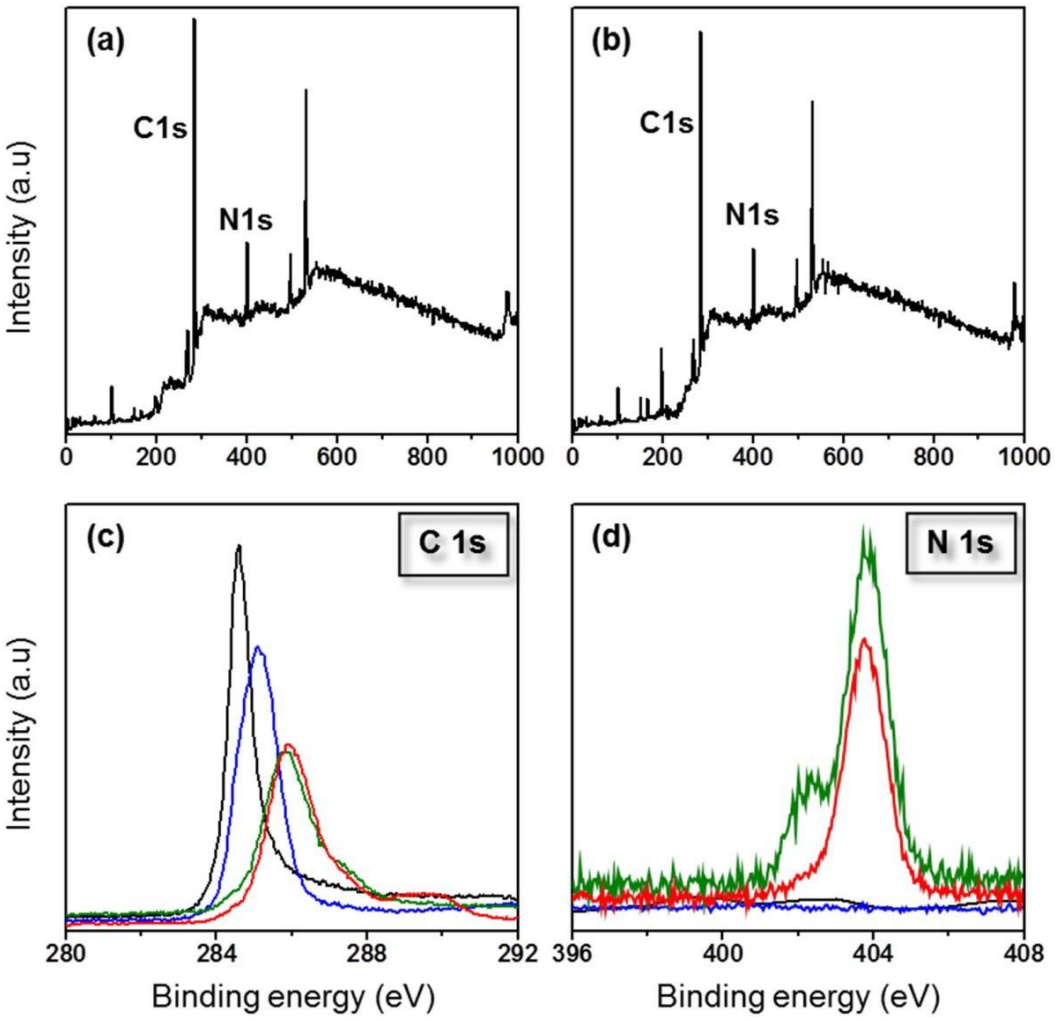

Figure S3. XPS survey spectra of (a) p-CNT/PSS/PAH and (b) p-CNT/PSS/PAH/PAA. XPS spectra of (c) C 1s core-level and (d) N 1s core-level of MWCNTs (black lines), p-CNT/PSS (blue lines), p-CNT/PSS/PAH (green lines) and p-CNT/PSS/PAH/PAA (red lines).

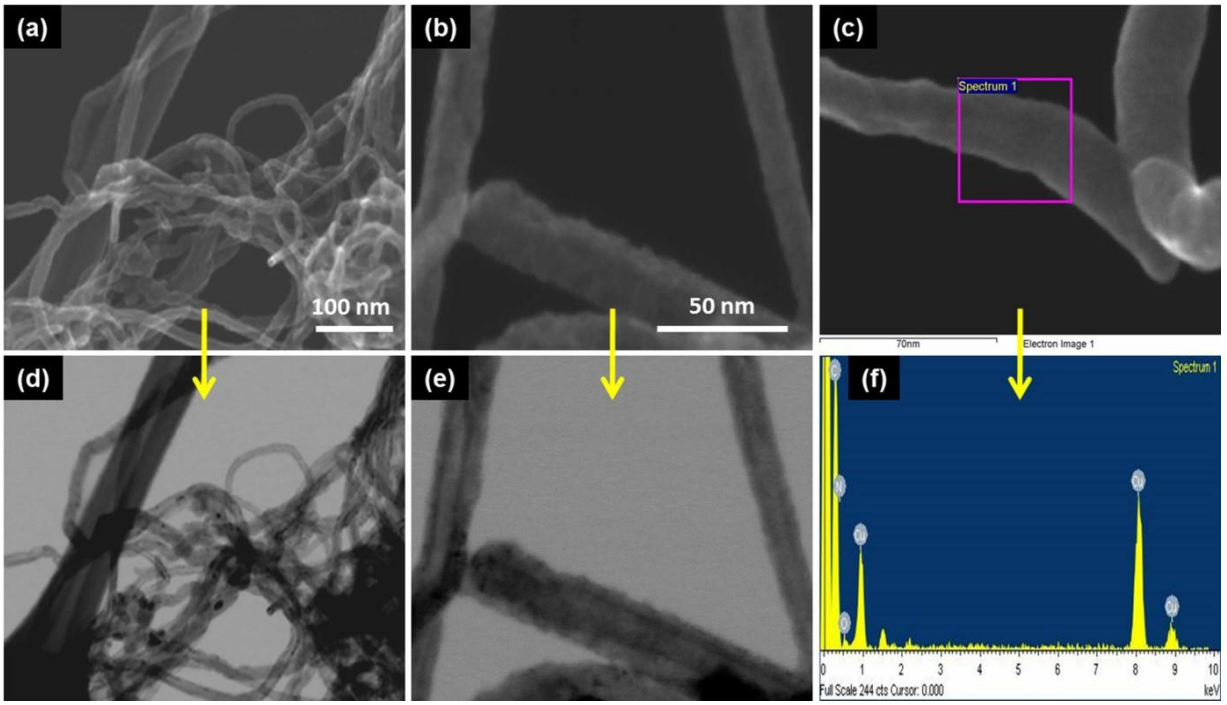

Figure S4. (a-c) Scanning electron (SE) mode and (d, e) transmission electron (TE) mode images of UHR-FESEM of p-CNT/PAH. (f) The EDS spectrum ensures the successful wrapping of PAH along the p-CNTs surface.

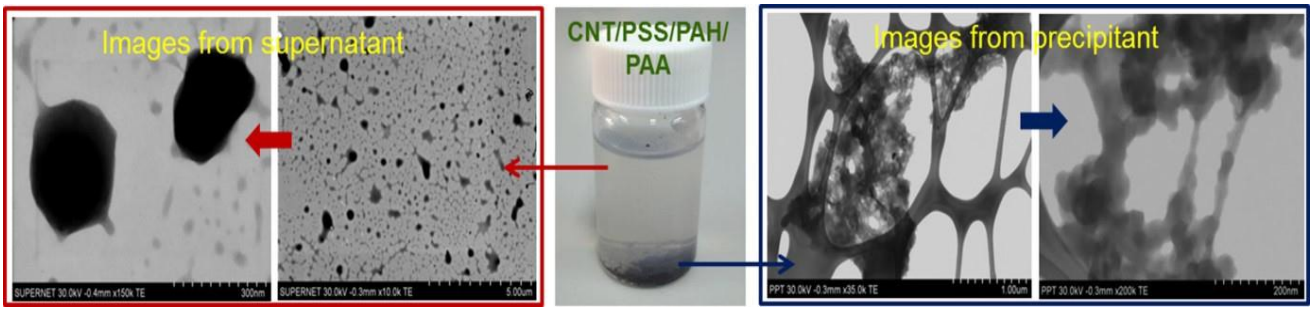

Figure S5. TEM micrographs obtained using supernatant (left) and highly aggregated precipitant (right) of p-CNT/PSS/PAH/PAA, which was prepared with a stoichiometric ratio.

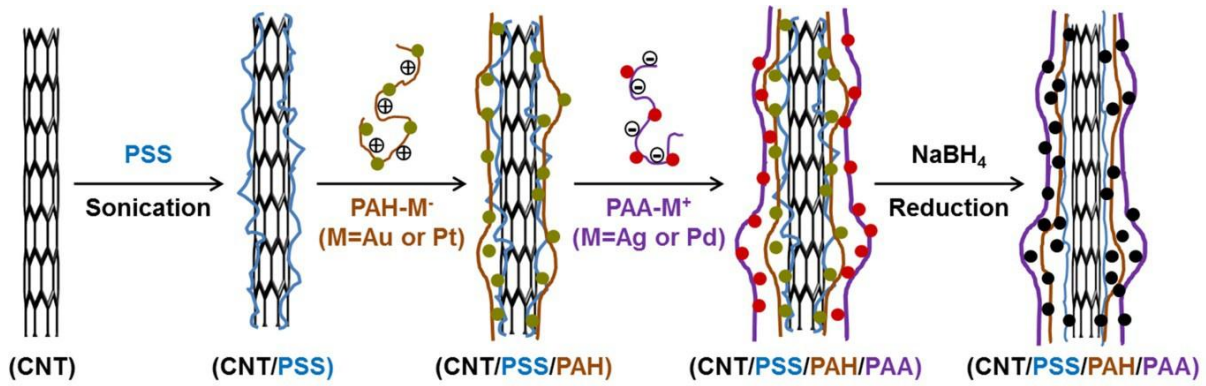

Figure S6. Schematics for the synthesis of bi- and tetra-metallic NP-embedded p-CNT/PSS/PAH/PAA.

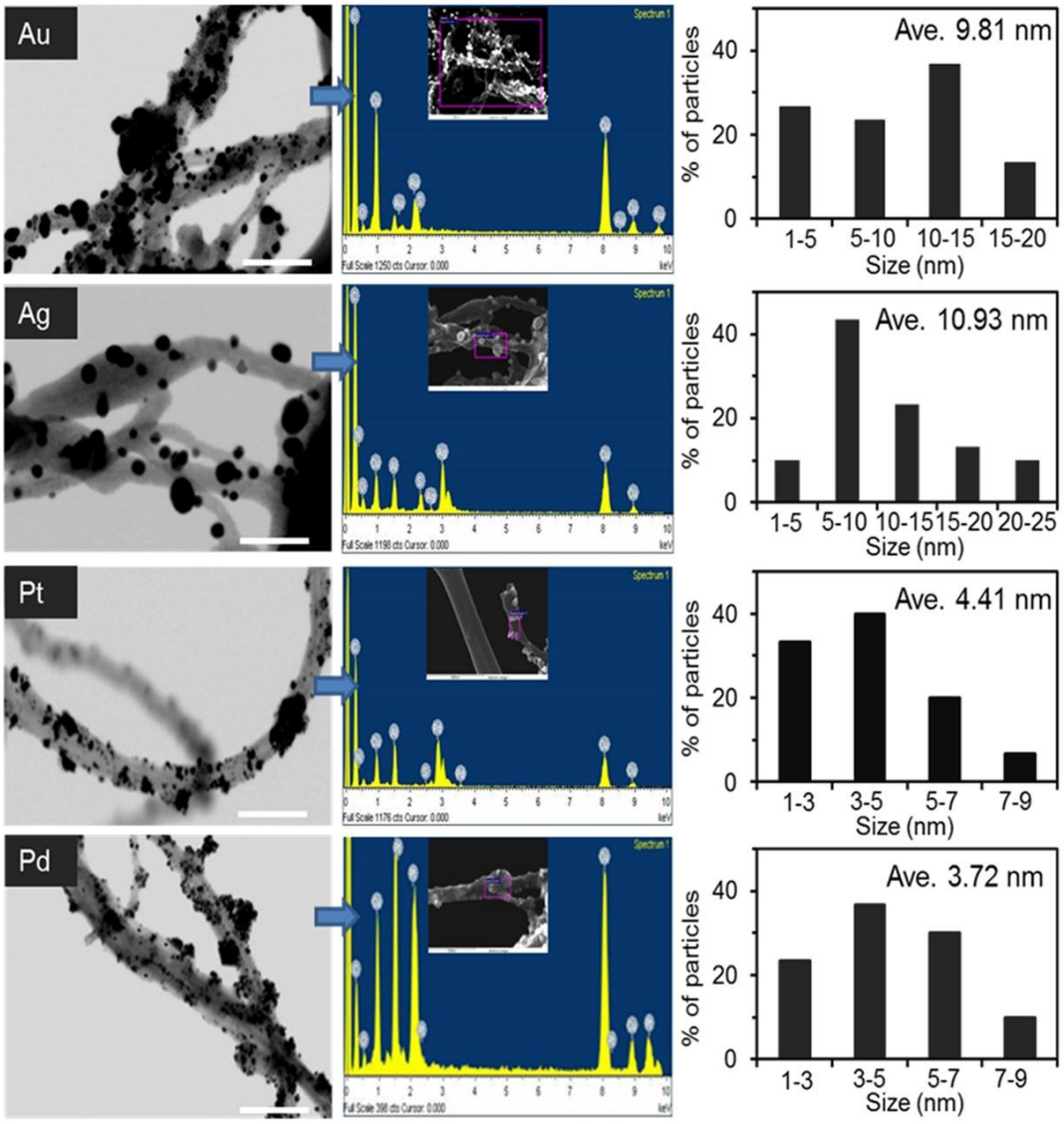

Figure S7. UHR-FESEM images for monometallic NPs-embedded p-CNT/PSS/PAH/PAA with the corresponding EDX spectra and size distribution data. Average size of the particles were calculated from randomly selected 30 metal NPs from TEM images. All scale bars represent 50 nm. In EDX spectra, Al and Cu peaks came from sample holder and copper grid, respectively. Any aggregation point was avoided for the calculation of the NP sizes.

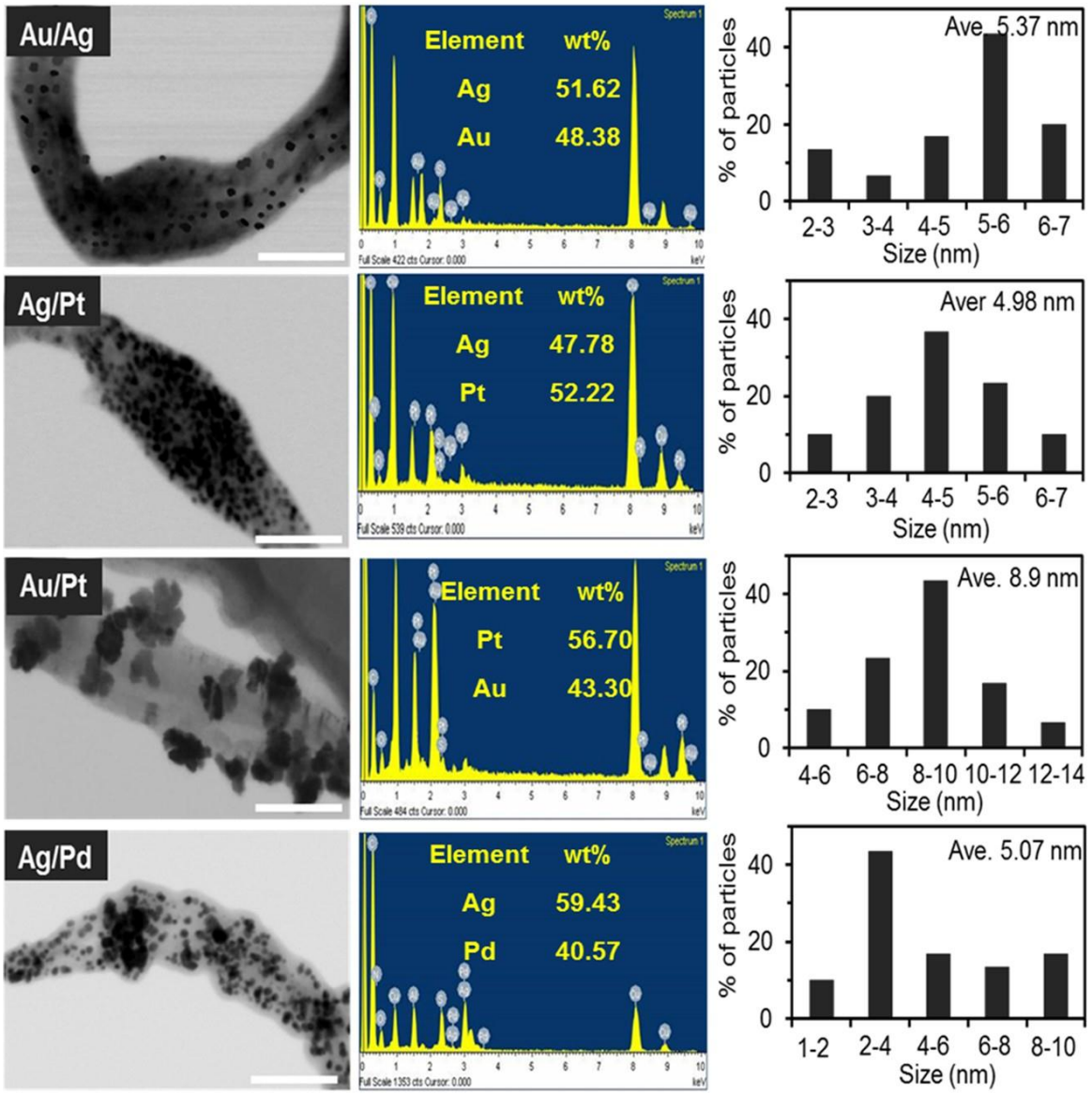

Figure S8. UHR-FESEM imagess for bi-metallic NPs-embedded p-CNT/PSS/PAH/PAA with the corresponding EDX spectra and size distribution data. Average size of the particles were calculated from randomly selected 30 metal NPs from TEM images. All scale bars represent 50 nm. In EDX spectra, Al and Cu peaks came from sample holder and copper grid, respectively. Any aggregation point was avoided for the calculation of the NP sizes. Comparative wt% ratio of various types of metal in p-CNT/PSS/PAH/PAA were obtained from EDX spectra.

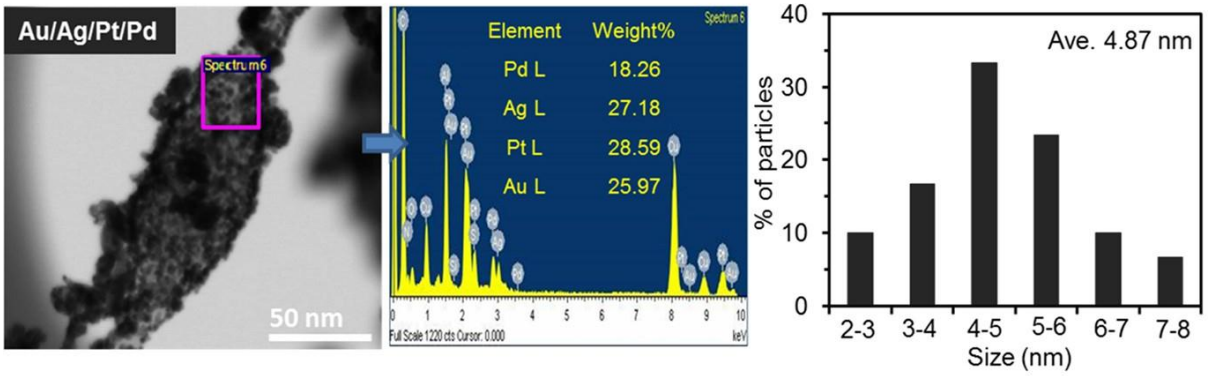

Figure S9. UHR-FESEM images for tetra-metallic NPs-embedded p-CNT/PSS/PAH/PAA with the corresponding EDX spectra and size distribution data. Average size of the particles were calculated from randomly selected 30 metal NPs from TEM images. All scale bars represent 50 nm. In EDX spectra, Al and Cu peaks came from sample holder and copper grid, respectively. Any aggregation point was avoided for the calculation of the NP sizes. Comparative wt% ratio of various types of metal in p-CNT/PSS/PAH/PAA were obtained from EDX spectra.

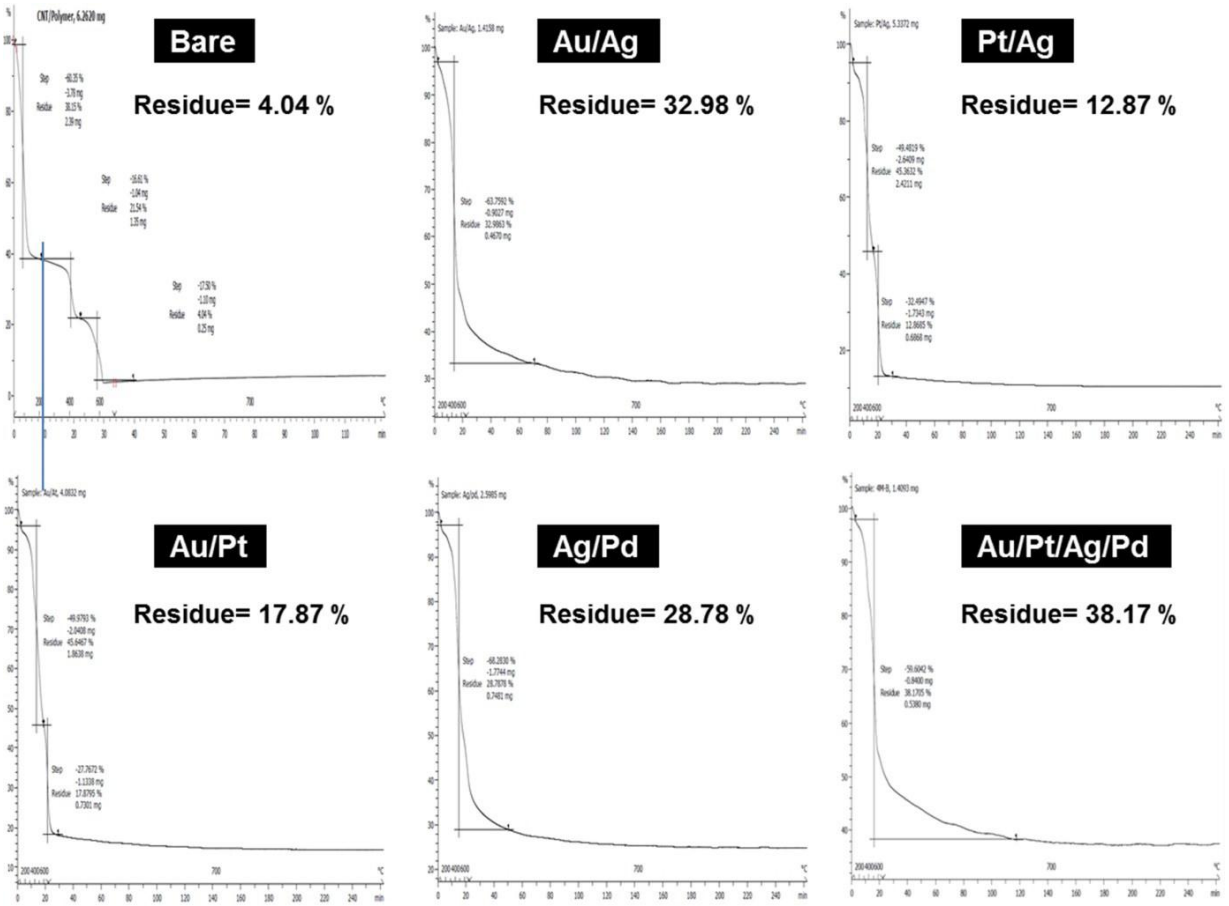

Figure S10. TGA data showing the loading amount (%) of metal NPs in bi-, and tetra-metallic system onto the p-CNT/PSS/PAH/PAA**.**

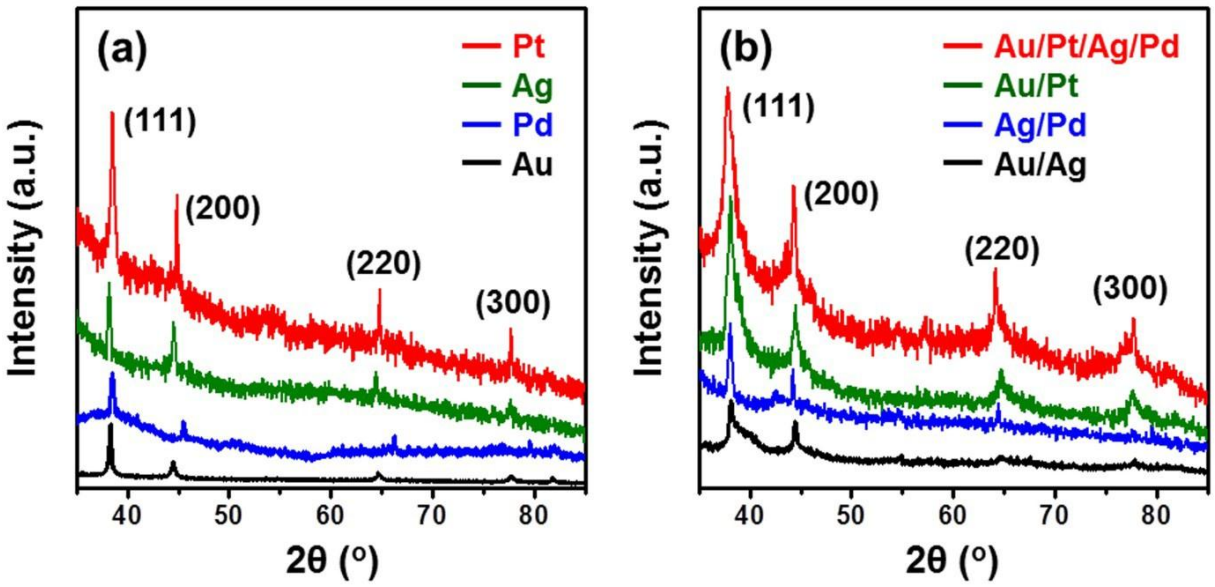

Figure S11. X-ray diffraction patterns of (a) monometallic NP- and (b) alloy-typed bi- and tetrametallic NP-embedded p-CNT/PSS/PAH/PAA.

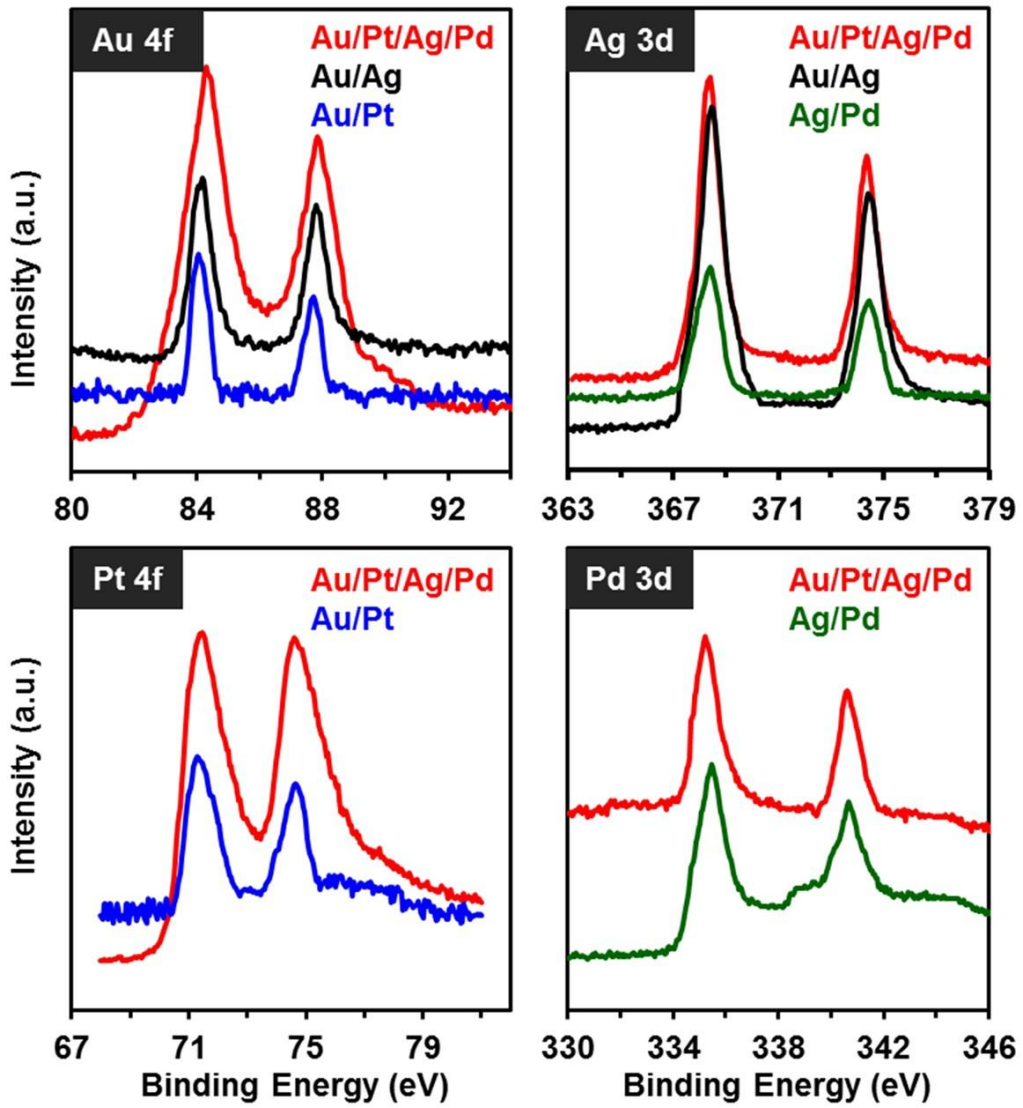

Figure S12. XPS spectra for alloy-typed bi- and tetrametallic NP-embedded p-CNT/PSS/PAH/PAA.

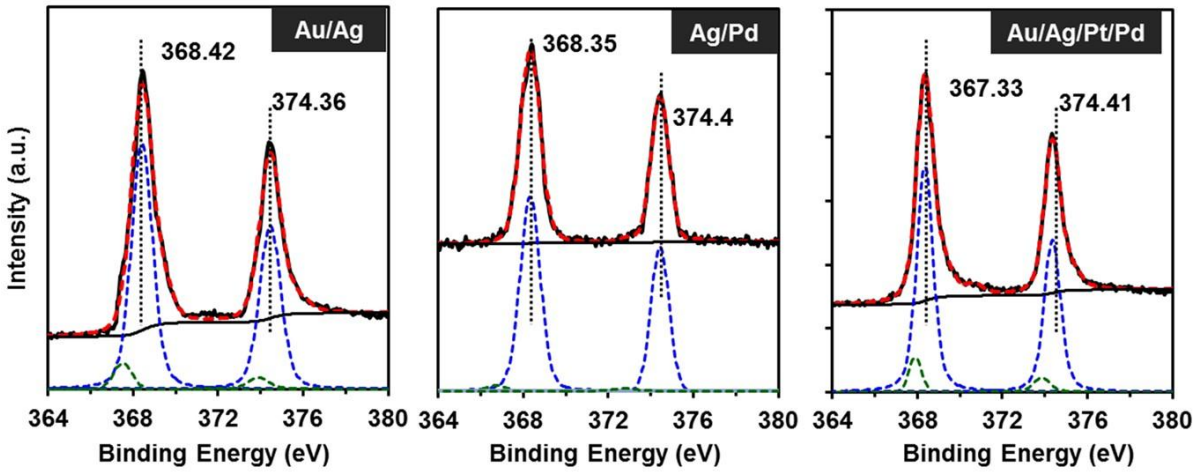

Figure S13. Deconvoluted XPS (Ag 3d) data for AgNP-contained p-CNT/PSS/PAH/PAA.

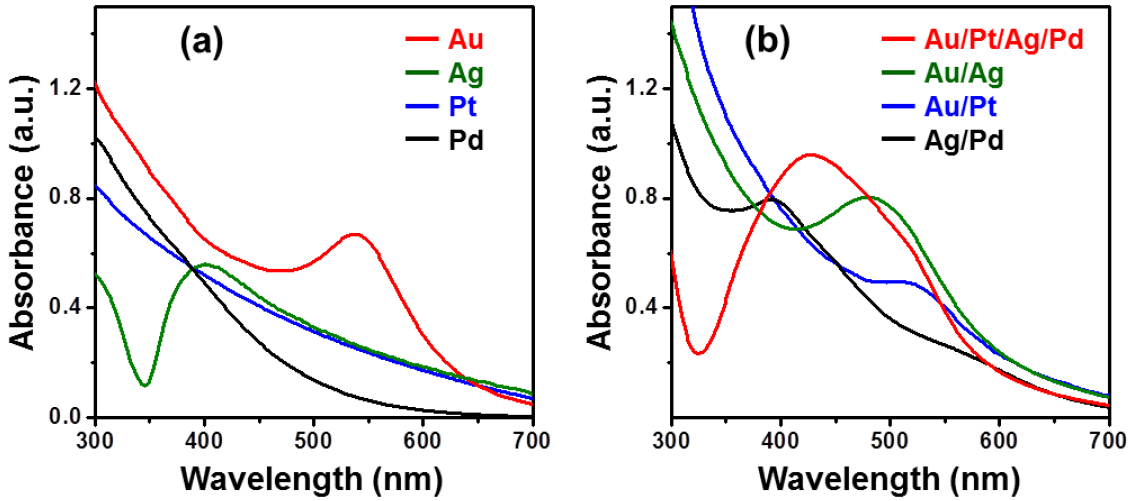

Figure S14. UV-absorbance spectra for (a) monometallic NP- and (b) alloy-typed bi- and tetrametallic NP-embedded p-CNT/PSS/PAH/PAA.

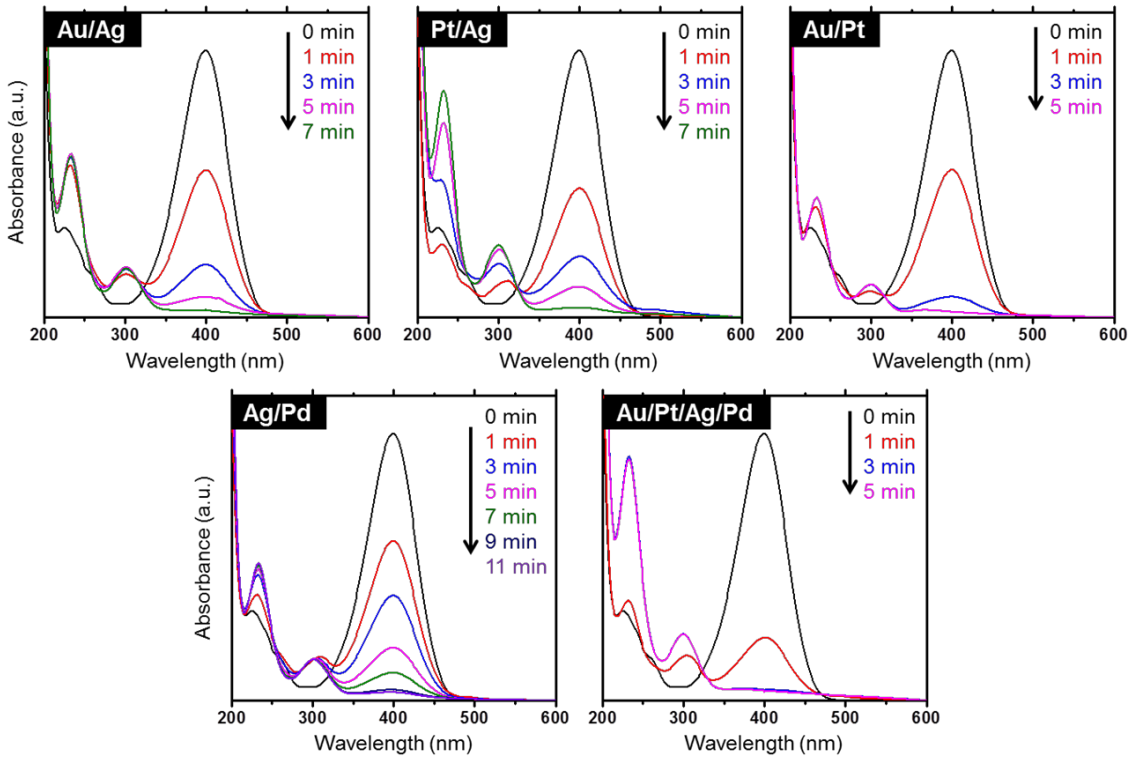

Figure S15. The time-dependent UV-Vis absorption spectral changes for the reduction of 4-NPh in the presence of bi- and tetrametallic NP-CNT/PSS/PAH/PAA.

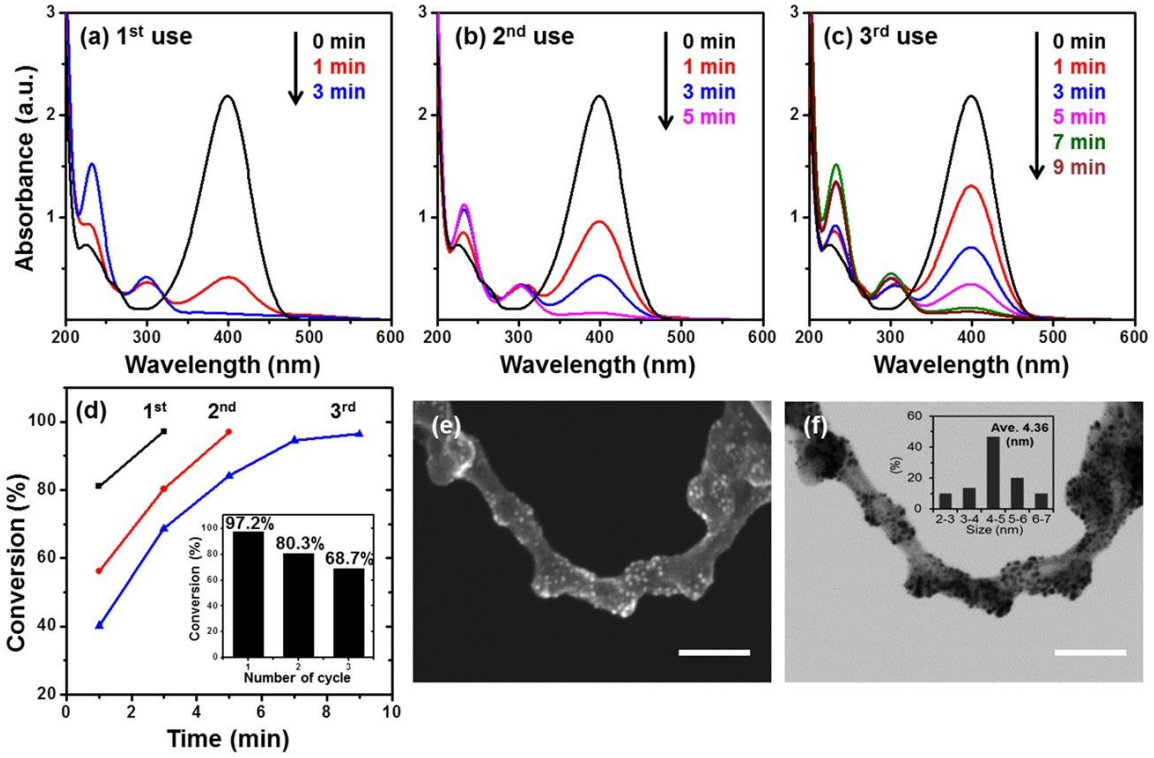

Figure S16. Representative UV-absorbance for the reusability test of p-CNT/PSS/PAH/PAA-M (M=Au/Ag/Pt/Pd) for the reduction of 4-NPh after completing (a) the first, (b) the second and (c) the third use. (d) The conversion rates of 4-NPh reduction for each use. (e and f) UHR-FESEM images of the catalysts after the third use in SE mode (e) and TE mode (f). Insets of (d) and (f) are the conversion % of 4-NPh reduction after 3 min. and size distribution of metal NPs after the third use, respectively. Scale bars represent 50 nm.

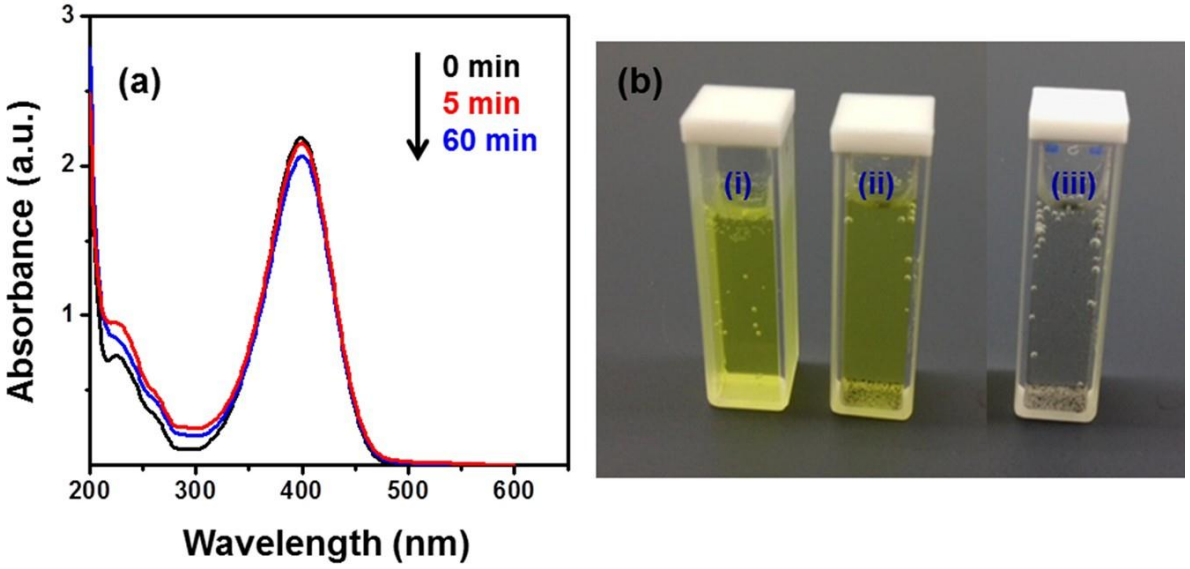

Figure S17. (a) The time-dependent UV-vis absorption spectral changes for the reduction of 4-NPh in the presence of p-CNT/PSS/PAH/PAA and (b) photographs of 4-NPh/$NaBH_4$ solution (i) as it is, (ii) in the presence of p-CNT/PSS/PAH/PAA after 60 min, and (iii) in the presence of p-CNT/PSS/PAH/PAA –*M* (*M* = Au/Pt/Ag/Pd) after 3 min.

Table S1. Residual metal component wt% of p-CNT/PSS/PAH/PAA-*M* (*M*=Au/Ag, Pt/Ag, Au/Pt, Ag/Pd and Au/Pt/Ag/Pd) obtained by TGA analysis. Net wt% of metal content was calculated by subtracting residual wt% of bare p-CNT/PSS/PAH/PAA from p-CNT/PSS/PAH/PAA-*M*.

M	Initial wt (mg)	Residual wt (mg)	Residual wt (%)	Net wt (%) of metal
none	6.26	0.25	4.04	-
Au/Ag	1.42	0.46	32.98	28.94
Pt/Ag	5.34	0.69	12.87	8.83
Au/Pt	4.08	0.73	17.87	13.83
Ag/Pd	2.60	0.75	28.78	24.74
Au/Pt/Ag/Pd	1.41	0.54	38.17	34.13

Table S2. Summary of XPS results with comparative mass % of constituent metal NPs in p-CNT/PSS/PAH/PAA-*M*.

M	Peak	BE (eV)	Raw RSF	Atomic Mass	Atomic Conc. (%)	Mass Conc. (%)
Au/Ag/Pt/Pd	Au 4f	84.25	6.250	196.967	21.10	26.59
	Pt 4f	71.45	5.575	195.084	22.05	29.46
	Ag 3d	368.33	5.987	107.878	31.32	25.24
	Pd 3d	335.36	5.356	106.534	25.53	18.71
Au/Ag	Au 4f	84.15	6.250	196.967	46.72	47.63
	Ag 3d	368.41	5.987	107.878	53.28	52.37
Au/Pt	Au 4f	84.10	6.250	196.967	41.71	42.78
	Pt 4f	71.35	5.575	195.084	58.29	57.22
Ag/Pd	Ag 3d	368.35	5.987	107.878	60.16	60.46
	Pd 3d	335.25	5.356	106.534	39.84	39.54